coatings

MDPI

Article

Effect of Doping Content of MgO on Solar Absorptivity to IR Emissivity Ratio of Al_2O_3 Coatings

Han Zhu [1,2], Weize Wang [1,*], Dongdong Ye [3], Ting Yang [1], Dongpeng Li [1], Min Yang [1], Baohan Yuan [1] and Yihao Wang [1]

[1] Key Laboratory of Pressure System and Safety, Ministry of Education, School of Mechanical and Power Engineering, East China University of Science and Technology, No. 130 Meilong Road, Shanghai 200237, China
[2] China Coal Xinji Lixin Power Generation Co., Ltd., Bozhou 236000, China
[3] School of Artificial Intelligence, Anhui Polytechnic University, Wuhu 241000, China
* Correspondence: wangwz@ecust.edu.cn; Tel.: +86-21-6425-2819

Abstract: High-emissivity coatings are often used on the surfaces of solar probes to block heat from the sun. Therefore, improving the thermal control ability is the standard for determining the quality of the coatings. In this study, MgO was doped into Al_2O_3 to improve the thermal control ability of the coatings and to analyse the effect of different MgO doping contents. The solar absorptivity to infrared (IR) emissivity ratio (α/ε) was used to evaluate the thermal control ability of the coatings. The results showed that 5 wt.% MgO doping content is the best choice. The main reason for the change in α/ε is related to the doping of MgO, which affects the grain size of Al_2O_3.

Keywords: solar probe; solar absorptivity to infrared emissivity ratio; grain size

Citation: Zhu, H.; Wang, W.; Ye, D.; Yang, T.; Li, D.; Yang, M.; Yuan, B.; Wang, Y. Effect of Doping Content of MgO on Solar Absorptivity to IR Emissivity Ratio of Al_2O_3 Coatings. *Coatings* **2022**, *12*, 1891. https://doi.org/10.3390/coatings12121891

Academic Editor: Ajay Vikram Singh

Received: 10 November 2022
Accepted: 1 December 2022
Published: 5 December 2022

1. Introduction

Solar activity affects humans in various ways. Therefore, there is a need to explore the sun to analyse solar activity over time. In 2018, NASA successfully launched the Parker solar probe, which broke historical records by becoming the first object to approach close to the sun. Owing to the short distance between the Parker solar detector and the sun, the probe technology utilises a set of high-temperature-resistant thermal protection systems for protection against the high temperatures (2500 °F) and strong radiation flow generated by the sun during the operation of the detector [1,2].

The composition of a thermal protection system, such as a thermal protective coating, is complex. The thermal protective coating must not only reflect most of the visible solar radiation but also emit residual energy in the infrared region, which significantly reduces the temperature inside the spacecraft [3]. High-emissivity coatings are an important component of thermal protection coatings. They not only have the high-temperature resistance and good chemical stability of ordinary ceramic coatings but also have an excellent radiation and heat dissipation capacity. They have been favoured by researchers because of these advantages and are now widely used in metallurgical manufacturing, aerospace, architectural coatings, and several other technical fields [4–7].

As humans continue to explore the universe, the high-temperature resistance requirements of spacecraft are becoming stricter. Researchers have constantly introduced new substances and improved the existing material systems to enhance the emissivity of coatings. However, researchers have mainly focussed on increasing the emissivity to reduce the internal temperature of the coating, while ignoring the fact that absorptivity also affects the thermal protection effect of the coating [3]. Therefore, comprehensive consideration of the relationship between absorptivity and emissivity is required for a breakthrough in solving the temperature problem. In this study, α/ε was introduced as a parameter to measure the temperature-control effect of the coatings.

According to research data on high-emissivity coatings, most high-emissivity materials are based on compounds of oxygen, nitrogen, carbon, and boron [8,9], among which, oxides

are favoured because of their low price and good stability. Common oxides include Al_2O_3, Fe_2O_3, CuO, MnO_2, MgO, and Cr_2O_3. Among these materials, Al_2O_3 is widely used in several fields because of its excellent wear resistance [10], corrosion resistance [11], electrical insulation [12], and other properties [13]. With respect to using Al_2O_3 as a radiation-resistant optical material or as a shielding material in nuclear technology, Popov, A.I., et al. [14] and Ananchenko, D. V., et al. [15] studied the thermal stability and annealing mechanisms of radiation-induced defects. In the aerospace field, Al_2O_3 coatings also exhibit high-temperature stability, high infrared emissivity, and low solar absorptivity, all of which help to reduce the internal temperature of the spacecraft [3]. Atmospheric plasma spraying (APS) is the most widely used technology for Al_2O_3 coatings because of its wide range of spraying materials, dense coating structure, high bonding strength, and high control accuracy.

Common methods to improve the temperature-control effect of high-emissivity coatings include regulating the surface state, structure, and composition of the coatings [16]. According to a previous study, the best spraying distance for Al_2O_3 coatings was 110 mm, the best spraying power was 40 kW, and the best coating thickness was 140 μm. In addition, a large number of studies [17,18] have found that doping atoms with different radii will lead to defects in the lattice structure, and a variety of impurity energy levels will be introduced at the lattice defects, which will lead to electron transitions in the valence band, an increase in the number of free carriers, and, in turn, affect the emissivity of the coatings. Al^{3+} and Mg^{2+} have different radii, and MgO is a good sintering additive for Al_2O_3; thus, Kim et al. [19] added MgO to Al_2O_3 to improve the light transmittance of ceramic pellets.

In this work, to eliminate the influence of the microstructure, we prepared ceramic pellets to study the effect of MgO doping. The original powder was prepared by solid-phase synthesis and the spray-drying method was used to prepare the agglomerate powder. The particle size distribution of the powder was controlled between 15 and 45 μm. Finally, MgO-doped Al_2O_3 coatings were prepared by APS, and the differences between the ceramic pellets and coatings were analysed.

2. Experimental Procedures

2.1. Ceramic Preparation Method

In this study, to investigate the mechanism of material composition on α/ε, ceramic pellets were prepared to eliminate the influence of the coating microstructure. The particle sizes of the Al_2O_3 and MgO powder were in the range of 30–50 nm. To prevent the MgO powder from absorbing water, it was stored in a vacuum box. In addition, it was necessary to heat treat the powder at 350 °C before preparing the ceramic pellet, and the preparation speed was accelerated as much as possible during the preparation process. The steps for preparing the ceramic pellets are as follows. First, an electronic balance was used to weigh the Al_2O_3 and MgO powders with different weight ratios. The specific proportions are listed in Table 1. Secondly, the weighed raw powders with different proportions were placed in a ball milling tank, and absolute ethanol was used as the medium; the mass ratio of alumina grinding ball to raw powder was 2:1, and a planetary ball mill was used to grind and mix the powders for 24 h. Third, after grinding and mixing, the slurry was placed in the dryer and dried for 2 h. Fourth, an electronic balance was used to weigh 3 g of each of the dried powders, which were placed in a CIP-22M microisostatic press and maintained under a cold isostatic pressure of 300 MPa for 5 min. Finally, using an SXW-6-16 ceramic fibre furnace, the obtained pellets were sintered at 1550 °C for 72 h.

2.2. Coating Preparation Method

In this study, the spray-drying method was used to regranulate the original powder to obtain MgO-doped Al_2O_3 powders which were in the range of 15–45 μm. MgO-doped Al_2O_3 coatings were prepared via atmospheric plasma spraying (APS; F4-MB, Oerlikon Metco, Switzerland). A nickel-based alloy with a thickness of 3 mm and diameter of 25.4 mm was selected as the substrate. Prior to the deposition, the substrate was grit blasted

and ultrasonically cleaned with alcohol. Argon was the primary gas and hydrogen was the auxiliary gas used during spraying. Nitrogen was used as the powder gas, and the flow rate was 4 SLPM. The gas flow rates of argon and hydrogen were 35 and 5 SLPM, respectively (SLPM is standard lt/min, 1 SLPM = 1.699 m^3/h). During the spraying process, the spraying distance, spraying power, and transverse moving speed of the spray gun were 110 mm, 40 kW, and 140 μm, respectively.

Table 1. Composition of ceramic pellets.

Components	Sample 1 (wt.%)	Sample 2 (wt.%)	Sample 3 (wt.%)	Sample 4 (wt.%)	Sample 5 (wt.%)
Al_2O_3	100	99	97	95	90
MgO	0	1	3	5	10

2.3. Measurement of the Properties

An IRE-2 infrared radiation tester (Shanghai Institute of Technical Physics of the Chinese Academy of Sciences, Shanghai, China) and Lambda 950 spectrophotometer (Perkin Elmer Instruments Co., Ltd., Boston, USA) were used to measure the ε and α of the coatings and ceramics, respectively. The ε and α values of the coatings were measured in a dark and dry room. In addition, to avoid the influence of external noise, vibration, and other factors on the measurement results, the vibration and noise of the measurement environment were assessed before measurement. X-ray diffraction (XRD) was performed using an X-ray diffractometer (Rigaku Co., Ltd., Tokyo, Japan) to analyse the phase. The JADE 6.0 software was used to analyse the XRD patterns of the Al_2O_3 coatings with different MgO doping contents, and the porosity of the coatings was measured using the ImageJ software. Scanning electron microscopy (SEM) was performed using S-3400N (Hitachi Analytical Instruments Co., Ltd., Tokyo, Japan) to investigate the microstructures of every sample.

3. Result and Discussion

3.1. Effect of Doping Content of MgO on α/ε of Ceramic Pellet

MgO was used as a sintering aid to suppress the grain growth in Al_2O_3 [19]. Previous studies showed that the effects on α differ in changing the MgO doping content. When Al_2O_3 is doped with excessive MgO, a second phase ($MgAl_2O_4$) appears [20]. To explore the influence of different MgO doping contents on the α/ε values of Al_2O_3, several groups of experiments were designed in this study, and the parameters are listed in Table 1.

The MgO-doped Al_2O_3 ceramic pellets were sintered at 1550 °C, and their XRD patterns are shown in Figure 1. The results show that when the MgO content was 1 wt. %, only the diffraction peak of Al_2O_3 was observed, while no peak of MgO was detected. The Al_2O_3 peak shifted to the left (2θ = 25.4) because the ionic radius of Mg^{2+} is larger than that of Al^{3+}. With an increase in the Mg^{2+} content, the lattice constant of the cell increases, leading to a shifting of the Al_2O_3 peak towards lower 2θ values (towards the left) [21]. The $MgAl_2O_4$ phase was observed when the addition of MgO was greater than 1 wt.%, indicating that a chemical reaction occurred between Al_2O_3 and MgO during the sintering process. According to the literature [22], when the doping content is less than the critical value, MgO forms a solid solution with Al_2O_3. At this time, XRD cannot measure the diffraction peak of the impurities; when the addition of MgO is greater than the critical value, MgO reacts with Al_2O_3 to produce $MgAl_2O_4$.

The microstructures of the MgO-doped Al_2O_3 ceramic pellets are shown in Figure 2. The centre of the grain was selected and a horizontal line was drawn from the centre point. This was rotated clockwise by 15° each time and the average of the length was taken as the grain size. Figure 2a shows that the Al_2O_3 ceramic pellet without MgO addition and sintered at 1550 °C exhibited larger grains (5.681 μm), and the grain shape presented an equiaxed polygon with wide grain boundaries. Figure 2b shows that when the MgO content was 1 wt.%, the grain size (4.372 μm) decreased and the grain boundary was

relatively narrow. When the MgO content was equal to or greater than 3 wt.%, the grain boundary started to melt (Figure 2c–e). Therefore, MgO can effectively reduce the sintering temperature of the Al_2O_3 ceramic pellets. In addition, MgO reacts with Al_2O_3 to produce $MgAl_2O_4$, and the existence of spinel $MgAl_2O_4$ restrains grain growth.

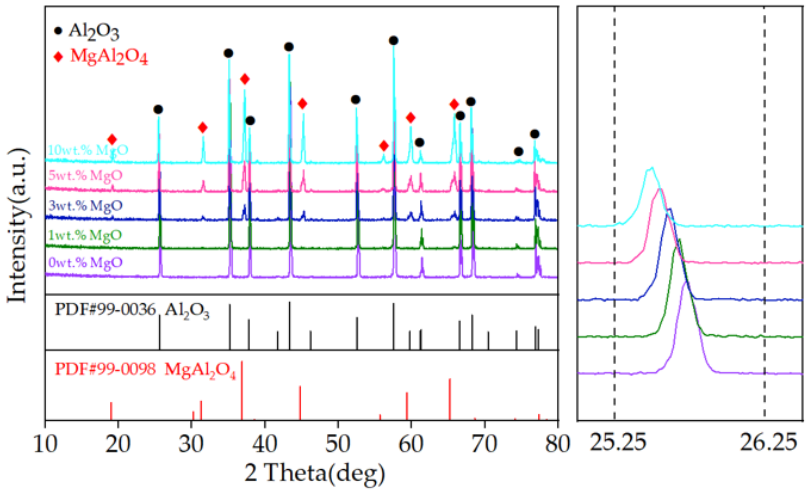

Figure 1. XRD patterns of MgO-doped Al_2O_3 ceramic pellets.

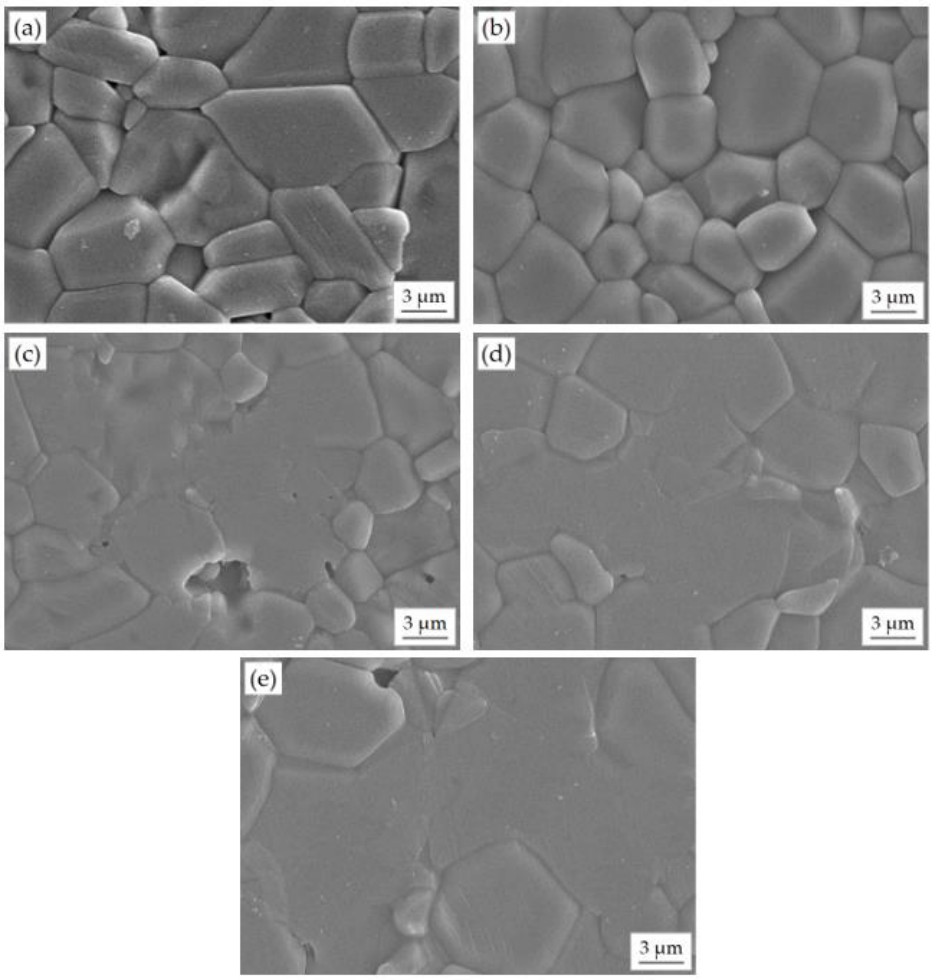

Figure 2. SEM images of the Al_2O_3 ceramic pellets with different MgO doping contents: (**a**) 0 wt.%; (**b**) 1 wt.%; (**c**) 3 wt.%; (**d**) 5 wt.%; (**e**) 10 wt.%.

The α and ε values of the MgO-doped Al_2O_3 ceramic pellets are shown in Figure 3. The ε value of the ceramic pellets increased when the addition of MgO was increased from 0 to 1 wt.% and remained relatively unchanged as the MgO content was increased from 1 to 10 wt.%. In addition, the α values exhibited a changing trend. The increase in ε is due to the introduction of MgO, which produces $MgAl_2O_4$. The spinel structure has the characteristics of high emissivity because doping causes lattice distortion, destroys the symmetry of the crystal form, and results in an asymmetric dipole vibration, thereby increasing ε [23]. When the MgO doping content was less than or equal to 1 wt.%, the α value of the ceramic pellet increased with increasing doping content. Combined with the SEM results of the ceramic pellets, it was found that, compared with the ceramic pellet without the addition of MgO, the grain size with a doping content of 1 wt.% was relatively small. A smaller grain size increased the contact area of the grain boundary. Thus, when light was introduced into the ceramics, the scattering effect of light became more visible, leading to an extension of the optical path and an increase in the α value of the ceramics. Therefore, when the doping content of MgO was between 0 and 1 wt.%, the main reason for the increase in the α value of the ceramic pellets was that doping with MgO restrained grain growth [19]. When the MgO doping content was greater than 1 wt.%, the α value of the ceramic pellets exhibited a downward trend, and when it was 5 wt.%, the corresponding α value was the smallest. In this process, the main reason for the decrease in α was that, although the smaller grain size led to an increase in grain boundaries, the phenomenon of grain boundary melting occurred, which reduced the scattering effect of the incident light, thereby reducing the α value of the Al_2O_3 ceramic pellets. When the MgO doping content was further increased, the α value of the ceramic pellets showed an increasing trend. This is because, although the grain boundary melting phenomenon was evident, the excessive doping content of MgO led to the formation of $MgAl_2O_4$, and the generated second phase became a new light scattering source, thereby increasing the α value of the Al_2O_3 ceramic pellets.

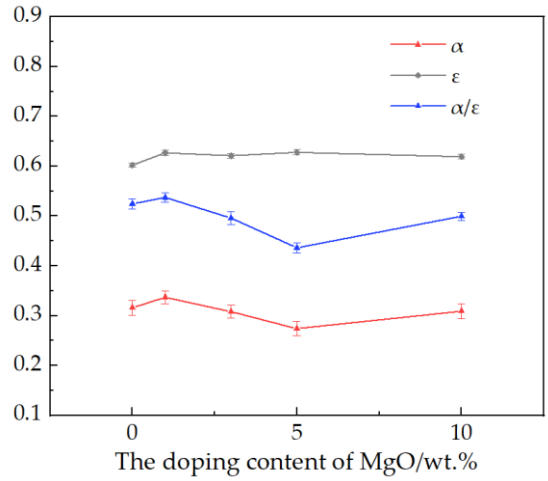

Figure 3. α/ε values of the Al_2O_3 ceramic pellets with different MgO doping contents.

3.2. Properties of MgO-Doped Al_2O_3 Spraying Powders

There are strict requirements for the fluidity and sphericity of the spraying powder because the thermally sprayed powder must be stably transported into the plasma flame flow. The morphology of the commonly used spray powder is generally spherical or nearly spherical. During the experiment, it was found that different particle sizes of the powder affect the thermal spraying properties [24].

The spray-drying method was used to regranulate the original powder to obtain a spherical powder. Because the surface morphology and particle size of each powder were approximately the same, Figure 4 shows the morphology of the typical MgO-doped Al_2O_3 powder after spray drying. The obtained powders had approximately similar particle sizes

ranging from 15–45 μm. In addition, some irregular shapes were observed, constituting a small percentage of the powder, which were caused by spherical powder crushing.

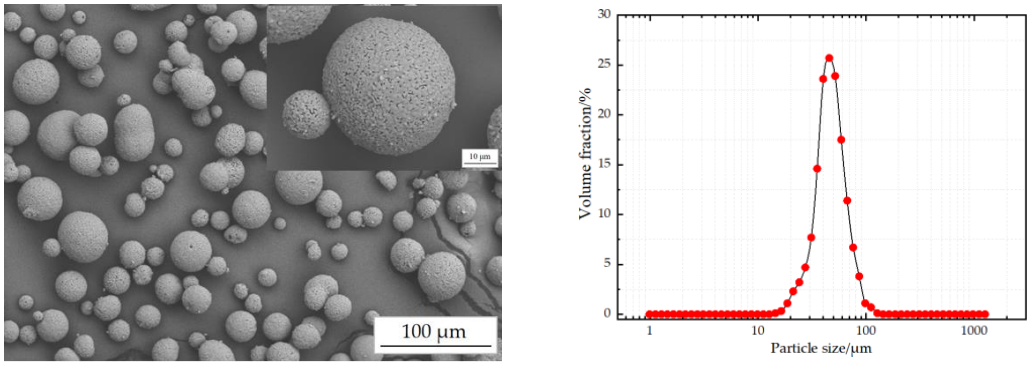

Figure 4. Morphology and size distribution of MgO-doped Al_2O_3 powder. (**a**) morphology of MgO-doped Al_2O_3 powder after spray drying. (**b**) particle sizes of MgO-doped Al_2O_3 powder after spray drying.

The XRD results of the phase of the powders with different MgO doping contents are shown in Figure 5. When the MgO doping content was 1 wt.%, only the diffraction peak of Al_2O_3 was observed and no peak of MgO was detected, which is consistent with the XRD results of the as-prepared ceramic pellets. This is because MgO reacts with Al_2O_3 to produce $MgAl_2O_4$. However, the content of $MgAl_2O_4$ is low, and its diffraction peak cannot be observed. When the MgO doping content was greater than 1 wt.%, the diffraction peak of $MgAl_2O_4$ was observed, because the $MgAl_2O_4$ content was so high that the peak could finally be detected in XRD.

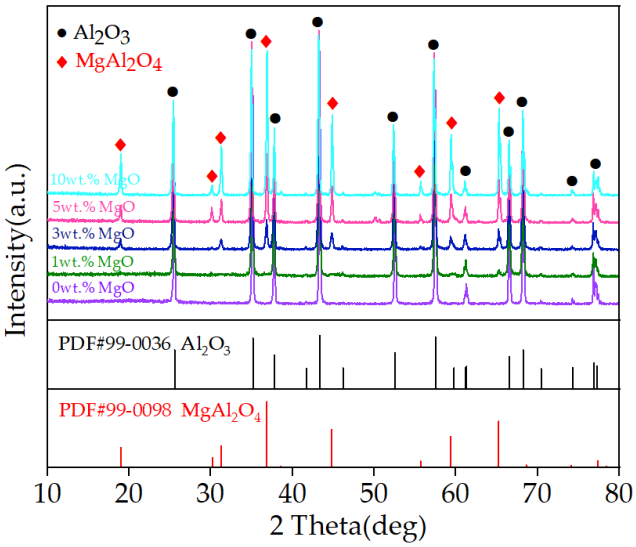

Figure 5. XRD patterns of the Al_2O_3 powders with different MgO doping contents.

3.3. Properties of MgO-Doped Al_2O_3 Coatings

Figure 6 shows the microstructures of the Al_2O_3 coatings with different MgO doping contents. The coatings exhibited a typical layered structure of plasma spraying, and the pores of the ceramic layer on the surface were evenly distributed. The porosity of the coatings exhibited a decreasing trend, with values of 10.12% (Figure 6a), 8.97% (Figure 6b), 8.13% (Figure 6c), 6.92% (Figure 6d), and 6.68% (Figure 6e).

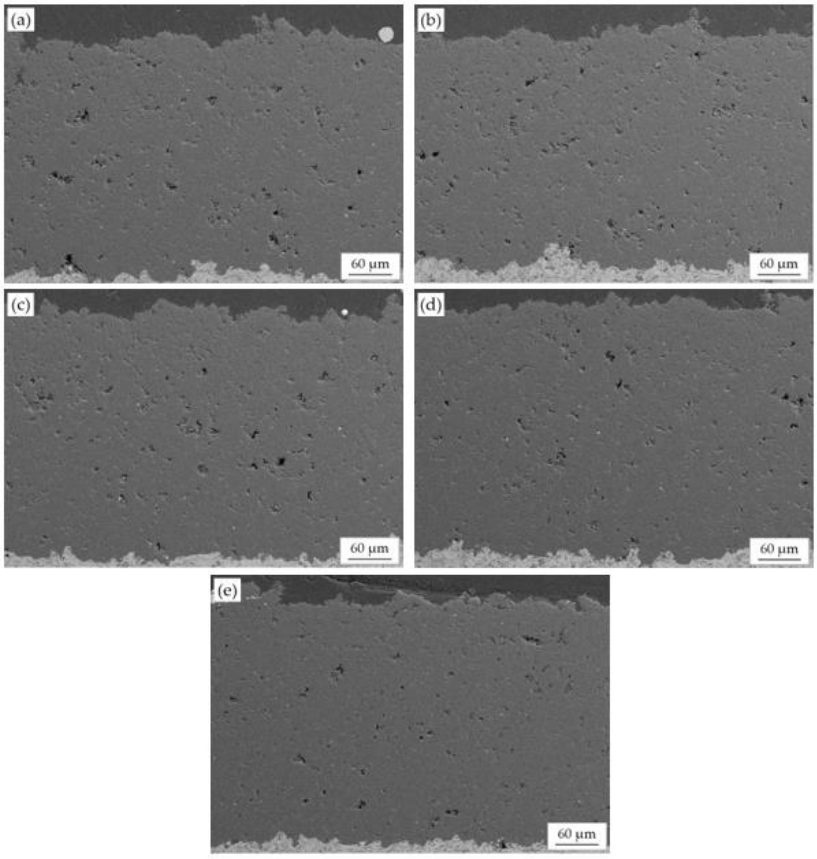

Figure 6. Microstructures of the Al_2O_3 coatings with different MgO doping contents: (**a**) 0 wt.%; (**b**) 1 wt.%; (**c**) 3 wt.%; (**d**) 5 wt.%; (**e**) 10 wt.%.

Figure 7 shows that the XRD pattern of the Al_2O_3 coating with a MgO doping content of 1 wt.% only exhibits the diffraction peak of Al_2O_3, and no peak of MgO was detected. When the MgO doping content was 3, 5, and 10 wt.%, the diffraction peaks of $MgAl_2O_4$ were observed. On comparing these results with those of the phase structures of the powders in Figure 5, it can be concluded that the phase structure of the powder and coating is the same, indicating that the thermal spraying process did not change the phase structure.

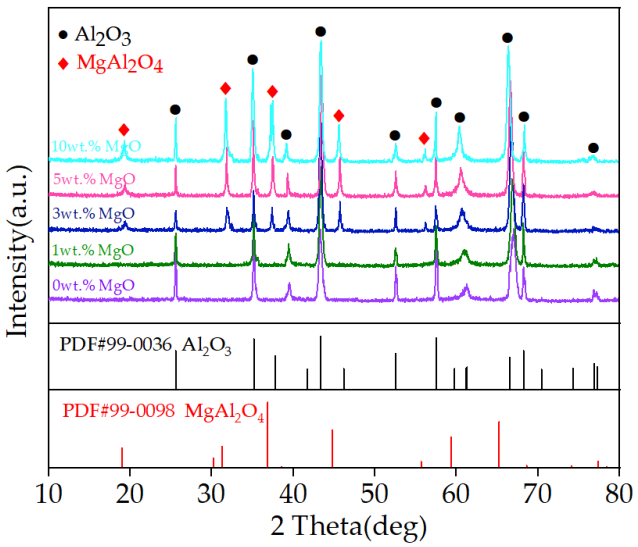

Figure 7. XRD patterns of Al_2O_3 coating with different MgO doping contents.

Figure 8 shows that the variation of α and ε of the MgO-doped Al_2O_3 coatings are quite different. When the MgO doping content was increased from 0 to 10 wt.%, the ε value was stable, that is, approximately 0.93. When the MgO doping content was less than or equal to 1 wt.%, the α values of the coatings increased with increasing doping content. According to our previous study, α increased with increasing porosity when the porosity was less than 9% and decreased when it was greater than 9% [25]. When the MgO doping content was greater than 1 wt.%, the α value decreased with increasing MgO doping content. The α value was the minimum when the MgO doping content was 5 wt.%. With a further increase in the MgO doping content, the α values of coatings showed an upward trend. On comparing these results with those of the ceramic pellets, it was found that the α/ε trend for both the ceramic pellets and coatings was consistent.

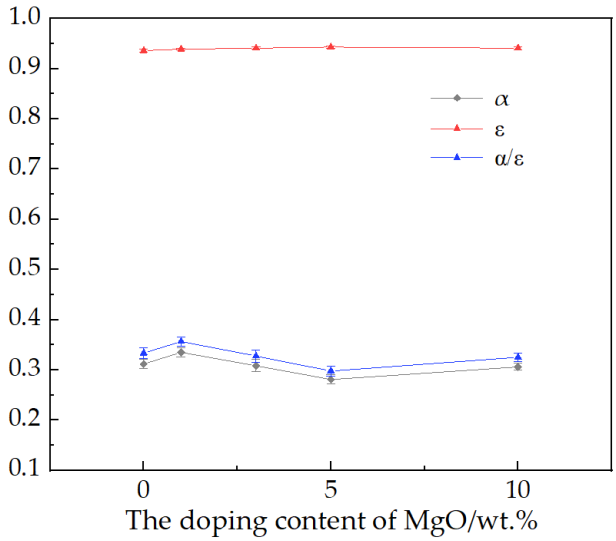

Figure 8. α/ε values of the Al_2O_3 coatings with different MgO doping contents.

On comparing the properties of the ceramic pellets and coatings, differences were clearly observed. First, the microstructures of the ceramic pellets were characterized as grains, while those of the coatings were laminar structures. Figure 6 shows that the porosities of the coatings are different. This can be analysed from the microstructures of the ceramic pellets. Figure 2 shows that Al_2O_3 without MgO doping has a larger grain size because MgO suppresses grain growth in Al_2O_3. When the spraying parameters were the same, the powders with a lesser MgO doping content were more difficult to melt. Hence, a greater porosity was observed in Figure 6a than in Figure 6b–e. As the MgO doping content increased, the porosity of the coatings decreased. However, similar porosities were observed in Figures 6d and 6e. This is attributed to the phenomenon of grain boundary melting. Grain boundary melting may have a greater influence on melting than grain size. Second, the XRD patterns of the ceramic pellets and coatings hardly showed any difference, mainly because APS is a transient cooling process, which may lead to the growth of different crystal planes. Third, both the α and ε values of the coatings exhibited a certain degree of increase. This is because the incident light can pass across the coating and reach the substrate. The substrate may reflect the light back into the coating, which may cause the coating to either absorb the light or transmit the reflected light to the outside.

4. Conclusions

In this study, Al_2O_3 was doped with different MgO contents to improve the thermal control ability of the Al_2O_3 coatings. First, to eliminate the influence of the microstructure, ceramic pellets were prepared to study the effect of MgO doping. It was found that doping with MgO influences the grain size of Al_2O_3 and excessive doping melts the grain boundary or even produces $MgAl_2O_4$. Second, solid-phase synthesis and the spray-drying method

were used to obtain the powders for plasma spraying. The spherical or nearly spherical powders had approximately similar particle sizes, ranging from 15 to 45 μm. Finally, APS was used to prepare the MgO-doped Al_2O_3 coatings. The α/ε trend for both the ceramic pellets and coatings was consistent; however, the accurate numerical values were not the same.

Author Contributions: Conceived and designed the experiments, H.Z. and W.W.; performed the experiments, H.Z., W.W., D.Y., T.Y., D.L., M.Y., B.Y. and Y.W.; analysed the data and wrote the paper, H.Z. All authors have read and agreed to the published version of the manuscript.

Funding: This research is sponsored by the National Natural Science Foundation of China (52175136, 52130511), Science Center for Gas Turbine Project (P2021-A-IV-002-002), The National High Technology Research and Development Program of China (2021YFB3702200), Key Research and Development Projects in Anhui Province (2022a05020004).

Institutional Review Board Statement: Not applicable.

Informed Consent Statement: Not applicable.

Data Availability Statement: Not applicable.

Conflicts of Interest: The authors declare no conflict of interest.

References

1. Fox, N.J.; Velli, M.C.; Bale, S.D.; Decker, R.; Driesman, A.; Howard, R.A.; Kasper, J.C.; Kinnison, J.; Kusterer, M.; Lario, D.; et al. The Solar Probe Plus Mission: Humanity's First Visit to Our Star. *Space Sci. Rev.* **2016**, *204*, 7–48. [CrossRef]
2. Guo, Y.P. Solar Probe Plus: Mission design challenges and trades. *Acta Astronaut.* **2010**, *67*, 1063–1072. [CrossRef]
3. King, D.E.; Drewry, D.G.; Sample, J.L.; Clemons, D.E.; Caruso, K.S.; Potocki, K.A.; Eng, D.A.; Mehoke, D.S.; Mattix, M.P.; Thomas, M.E.; et al. Alumina Optical Surface Heat Shield for Use in Near-Solar Environment. *Int. J. Appl. Ceram. Technol.* **2009**, *6*, 355–361. [CrossRef]
4. Brodu, E.; Balat-Pichelin, M.; Sans, J.L.; Freeman, M.D.; Kasper, J.C. Efficiency and behavior of textured high emissivity metallic coatings at high temperature. *Mater. Des.* **2015**, *83*, 85–94. [CrossRef]
5. Wu, Y.B.; Ma, X.F.; Zhang, H.Z.; Zhou, Y. A New High Emissivity Coating on Ni-Based Superalloy Substrate. *Rare Metal Mat. Eng.* **2016**, *45*, 588–592. [CrossRef]
6. Li, L.F.; Yu, K.; Zhang, K.H.; Liu, Y.F. Study of Ti-6Al-4V alloy spectral emissivity characteristics during thermal oxidation process. *Int. J. Heat Mass Transf.* **2016**, *101*, 699–706. [CrossRef]
7. Liu, Y.F.; Xie, J.L.; Luo, M.; Peng, B.; Xu, C.; Deng, L.J. The synthesis and optical properties of Al/MnO_2 composite pigments by ball-milling for low infrared emissivity and low lightness. *Prog. Org. Coat.* **2017**, *108*, 30–35. [CrossRef]
8. Li, J.F.; Luo, Z.P. Fabrication and performances of preceramic polymer-based high-temperature High emissivity coating. *J. Eur. Ceram. Soc.* **2020**, *40*, 5217–5225. [CrossRef]
9. Zhu, Z.Q.; Cheng, X.D.; Ye, W.P.; Min, J. Synthesis of $NiCr_2O_4$ spinel coatings with high emissivity by plasma spraying. *Int. J. Miner. Metall. Mater.* **2012**, *19*, 266–270. [CrossRef]
10. Yang, K.; Rong, J.; Liu, C.G.; Zhao, H.Y.; Tao, S.Y.; Ding, C.X. Study on erosion-wear behavior and mechanism of plasma-sprayed alumina-based coatings by a novel slurry injection method. *Tribol. Int.* **2016**, *93*, 29–35. [CrossRef]
11. Szczygiel, B.; Kolodziej, M. Composite Ni/Al_2O_3 coatings and their corrosion resistance. *Electrochim. Acta* **2005**, *50*, 4188–4195. [CrossRef]
12. Shao, F.; Zhuang, Y.; Ni, J.X.; Sheng, J.; Zhao, H.Y.; Tao, S.Y.; Yang, K. Comparison of the microstructural characteristics and electrical properties of plasma sprayed Al_2O_3 and Al_2O_3-Ca_2SiO_4 coatings immersed in deionized water. *Surf. Coat. Technol.* **2021**, *422*, 127530. [CrossRef]
13. Rangaraj, S.; Kokini, M. Interface thermal fracture in functionally graded zirconia-mullite-bond coat alloy thermal barrier coatings. *Acta Mater.* **2003**, *51*, 251–267. [CrossRef]
14. Popov, A.I.; Lushchik, A.; Shablonin, E.; Vasil'chenko, E.; Kotomin, E.A.; Moskina, A.M.; Kuzovkov, V.N. Comparison of the F-type center thermal annealing in heavy-ion and neutron irradiated Al_2O_3 single crystals. *Nucl. Instrum. Methods Phys. Res. Sect. B Beam Interact. Mater. At.* **2018**, *433*, 93–97. [CrossRef]
15. Ananchenko, D.V.; Nikiforov, S.V.; Kuzovkov, V.N.; Popov, A.I.; Ramazanova, G.R.; Batalov, R.I.; Bayazitov, R.M.; Novikov, H.A. Radiation-induced defects in sapphire single crystals irradiated by a pulsed ion beam. *Nucl. Instrum. Methods Phys. Res. Sect. B Beam Interact. Mater. At.* **2020**, *466*, 1–7. [CrossRef]
16. Song, G.P.; He, S.F.; He, F.; Yao, Y.T.; Li, J.J.; Li, M.W.; He, X.D. Effect of doping graphene oxide on the structure and properties of SiO_2 based high emissivity coatings. *J. Appl. Polym. Sci.* **2020**, *137*, 9. [CrossRef]
17. Wang, S.M.; Kuang, F.H. Sol-gel Preparation and Infrared Radiation Property of Boron-substituted Cordierite Glass-ceramics. *J. Mater. Sci. Technol.* **2010**, *26*, 445–448. [CrossRef]

18. Zhu, Y.L.; Liu, S.; Zhang, X.K.; Xiang, Y. Effects of Cr^{3+} Concentration on the Crystallinity and Optical Properties of Cr-Doped Al_2O_3 Powders by Solid-State Reaction Method. *IOP Conf. Ser. Mater. Sci. Eng.* **2018**, *382*, 022037. [CrossRef]
19. Kim, B.N.; Hiraga, K.; Morita, K.; Yoshida, H.; Kagawa, Y. Light scattering in MgO-doped alumina fabricated by spark plasma sintering. *Acta Mater.* **2010**, *58*, 4527–4535. [CrossRef]
20. Kim, B.N.; Hiraga, K.; Morita, K.; Yoshida, H. Microstructure and Optical Properties of MgO-Doped Transparent Alumina Manufactured by Spark Plasma Sintering. In *Preprints of Annual Meeting of The Ceramic Society of Japan*; The Ceramic Society of Japan: Gifu, Japan, 2010; Volume 654, pp. 2041–2044. [CrossRef]
21. Bak, T.; Nowotny, J.; Rekas, M.; Ringer, S.; Sorrell, C.C. Defect Chemistry and Electrical Properties of La(1-x)Sr(x)CoO(3-delta) IV. Electrical Properties. *Ionics* **2001**, *7*, 388–393. [CrossRef]
22. Zeng, Y.; Wang, F.; Liao, Q.L.; Liu, H.; Li, X.B. Synthesis and characterization of translucent MgO-doped Al_2O_3 hollow spheres in millimeter-scale. *J. Alloys Compd.* **2014**, *608*, 185–190. [CrossRef]
23. Tian, J.; Zhu, W.R.; Li, H.D. Infrared radiant emissivities of ceramics with spinel structure. *Int. J. Infrared Millim. Waves* **1993**, *14*, 1855–1863. [CrossRef]
24. Qiao, X.; Wang, Y.M.; Weng, W.X.; Liu, B.L.; Li, Q. Influence of pores on mechanical properties of plasma sprayed coatings: Case study of YSZ thermal barrier coatings. *Ceram. Int.* **2018**, *44*, 21564–21577. [CrossRef]
25. Zhu, H.; Wang, W.Z.; Yang, T.; Fang, H.J.; Ye, D.D.; Li, D.P. Study on Influencing Factors of Solar Absorptance to IR Emittance Ratio of Al_2O_3 Coating by Atmospheric Plasma Spraying. *Hot Work. Technol.* **2021**, *16*, 43. [CrossRef]